PNAS RESEARCH ARTICLE | BIOPHYSICS AND COMPUTATIONAL BIOLOGY ENGINEERING OPEN ACCESS

Dehydration-induced corrugated folding in *Rhapis excelsa* plant leaves

Kexin Guo[a], Mingchao Liu[a,b,1], Dominic Vella[c], Subra Suresh[a,d,e,1], and K. Jimmy Hsia[a,f,1]

Contributed by Subra Suresh; received November 17, 2023; accepted February 28, 2024; reviewed by Chiara Daraio and M. Taher A. Saif

Plant leaves, whose remarkable ability for morphogenesis results in a wide range of petal and leaf shapes in response to environmental cues, have inspired scientific studies as well as the development of engineering structures and devices. Although some typical shape changes in plants and the driving force for such shape evolution have been extensively studied, there remain many poorly understood mechanisms, characteristics, and principles associated with the vast array of shape formation of plant leaves in nature. Here, we present a comprehensive study that combines experiment, theory, and numerical simulations of one such topic—the mechanics and mechanisms of corrugated leaf folding induced by differential shrinking in *Rhapis excelsa*. Through systematic measurements of the dehydration process in sectioned leaves, we identify a linear correlation between change in the leaf-folding angle and water loss. Building on experimental findings, we develop a generalized model that provides a scaling relationship for water loss in sectioned leaves. Furthermore, our study reveals that corrugated folding induced by dehydration in *R. excelsa* leaves is achieved by the deformation of a structural architecture—the "hinge" cells. Utilizing such connections among structure, morphology, environmental stimuli, and mechanics, we fabricate several biomimetic machines, including a humidity sensor and morphing devices capable of folding in response to dehydration. The mechanisms of corrugated folding in *R. excelsa* identified in this work provide a general understanding of the interactions between plant leaves and water. The actuation mechanisms identified in this study also provide insights into the rational design of soft machines.

plant morphology | leaf folding | dehydration | biomimetics | biomechanics

Significance

Plant leaf morphogenesis give rise to a wide variety of shapes, and these leaves exhibit adaptive responses to environmental changes. Understanding such phenomena not only provides insights into how plants adapt to and overcome environmental challenges but also offers novel approaches to developing biomimetic structures and engineered devices. Here, we study a specific shape-morphing phenomenon—dehydration-induced corrugated folding in the leaves of *Rhapis excelsa*. Through integrated experimental measurements, simulations, and modeling, we identify the mechanisms underlying the leaf's response to water stress through differential deformation between the "hinge cells" and major veins. Drawing inspiration from these adaptive morphing mechanisms, we demonstrate examples of biomimetic soft machines that are autonomously capable of shape changes in response to water evaporation or rehydration.

Shape-morphing is a remarkable phenomenon found in plants, and it allows them to change their shapes in response to environmental cues (1). This adaptive feature has evolved over time in plants to cope with ever-changing natural surroundings (2). Among plant structures, the leaf is particularly noteworthy in its capacity for shape-morphing by recourse to various modes of mechanical deformation (3, 4). Examples include

- folding of *Mimosa pudica* whose leaves, comprising up to 20 leaflets along its midrib, protect themselves from environmental stimuli and predators when touched by modulating the turgor pressure (5);
- snap-through buckling of *Dionaea muscipula*, a carnivorous plant commonly known as the Venus flytrap, that traps insects and other small prey by closing in on them through the rapid snapping of its leaves (6);
- curling or waving in a wide range of plant leaves, such as *Selaginella lepidophylla*, a species of desert plant that survives extreme desiccation and revives normal metabolic functions upon rehydration (7); and
- rolling of *Rhododendron* (8), whose flat, oblong-shaped leaves roll up to a tubular, cigar-like shape in response to a drop in ambient temperature.

The deformation processes described in the foregoing examples occur as plant tissues, inflated by turgor pressure, respond to accumulated residual stresses, often relying on hydroresponsive mechanisms (9–11). The principles underlying these morphing behaviors in plants have served as inspiration for the development of stimuli-responsive artificial structures (12–14). These bioinspired structures have also proven to be highly valuable in a wide range of applications, including mechanical metamaterials, soft robotics, biomimetic actuators, deployable space structures, and biomedical devices (15–18). Other examples of biomimetic applications include engineered materials made of plant-based building blocks such as soft nonallergenic microgels which are derived from hard pollen grains through a process similar to traditional soap making (19). Autonomously hygromorphing and self-propelling soft robotic structures made of pollen-based materials have been designed and demonstrated in applications such as

Author contributions: M.L., S.S., and K.J.H. designed research; K.G., M.L., and D.V. performed research; K.G., M.L., D.V., S.S., and K.J.H. analyzed data; and K.G., M.L., D.V., S.S., and K.J.H. wrote the paper.

Reviewers: C.D., California Institute of Technology; and M.T.A.S., University of Illinois Urbana-Champaign.

The authors declare no competing interest.

[1]To whom correspondence may be addressed. Email: m.liu.2@bham.ac.uk, ssuresh@mit.edu, or kjhsia@ntu.edu.sg.

This article contains supporting information online at https://www.pnas.org/lookup/suppl/doi:10.1073/pnas.2320259121/-/DCSupplemental.

Published April 8, 2024.

digital printing of self-morphing structures (20, 21) with the capability to repeatedly print and erase content on the same sheet of paper multiple times (22), as well as plant-based substrate materials for flexible green electronics (23).

Plants encounter various environmental conditions, and one crucial factor influencing their morphological and behavioral characteristics is water supply (9, 24). In this regard, water plays a significant role in the intricate morphological changes and movements exhibited by plants. Some of these mechanisms arise in response to active control of the distribution of water within plant tissues to induce or modulate mechanical deformation (25). This active regulation allows local swelling or shrinking of specific regions of plant tissues, resulting in remarkable shape changes. For example, the well-known folding of leaflets in *M. pudica* is achieved by ionically mediated water migration in the pulvinus between the extensor and the flexor motors (26, 27). Moreover, the hydraulic condition of a plant can lead to passive shape-morphing when nonuniform cellular structures or mechanical constraints are present (9). Pine cone scales provide a notable example of this phenomenon, as they open or close in response to changes in relative humidity by tuning the angle of the scales; this behavior results from the synergy between water content and structural properties of the scales (28). Additionally, the undulatory coiling motion of grass awns in response to humidity changes showcases their ability to utilize hygroscopic properties to fine-tune biological functions (29, 30). Understanding the interplay among water availability, plant tissues, and the resulting shape changes offers valuable insights into the remarkable adaptability of plants in their natural environments. By analyzing and imitating nature's strategies, engineering solutions and materials design principles can be developed across diverse fields (31, 32).

In engineering, foldable components are widely employed in robotics, space structures, and architectural applications in view of their many appealing characteristics including autonomous morphing capability, ease of transport, and reversibility of shape and deformation. These structures require a discontinuous change of curvature at the folding hinge to realize effective folding while maintaining minimal strain in other parts of the structure. Current engineering solutions for foldable structures often utilize origami design (33) or mechanical hinges (34), involving rigid components and complex deployment mechanisms. Folding-type morphing behavior is unusual in nature. While most leaves display a flat thin-shelled lamina, many species tend to exhibit curling- or rolling-type deformations upon dehydration (1). One example is the well-known rolling behavior of Poaceae leaves from the excess shrinking of water-storing bulliform cells or sometimes termed hinge cells (35, 36). However, certain plant species exhibit folding capability in their leaves, particularly in the palm family whose leaf blades possess a corrugated morphology with ridges forming along the leaf veins. This structure allows spontaneous hinge-type folding behavior upon dehydration. Corrugated leaf folding, therefore, requires a different structural mechanism, which remains poorly understood.

In this paper, we provide a detailed study of folding upon dehydration in *Rhapis excelsa* (family Arecaceae) also known as broadleaf lady palm or bamboo palm (Fig. 1). This is a widely cultivated palm species with a typical corrugated leaf morphology. We specifically chose this species for our investigation to focus on the role of a particular tissue component—the "hinge" cells (HCs)—in modulating the folding behavior. We present a systematic study of dehydration-induced corrugated leaf folding in *R. excelsa* by first characterizing the folding deformation in response to water

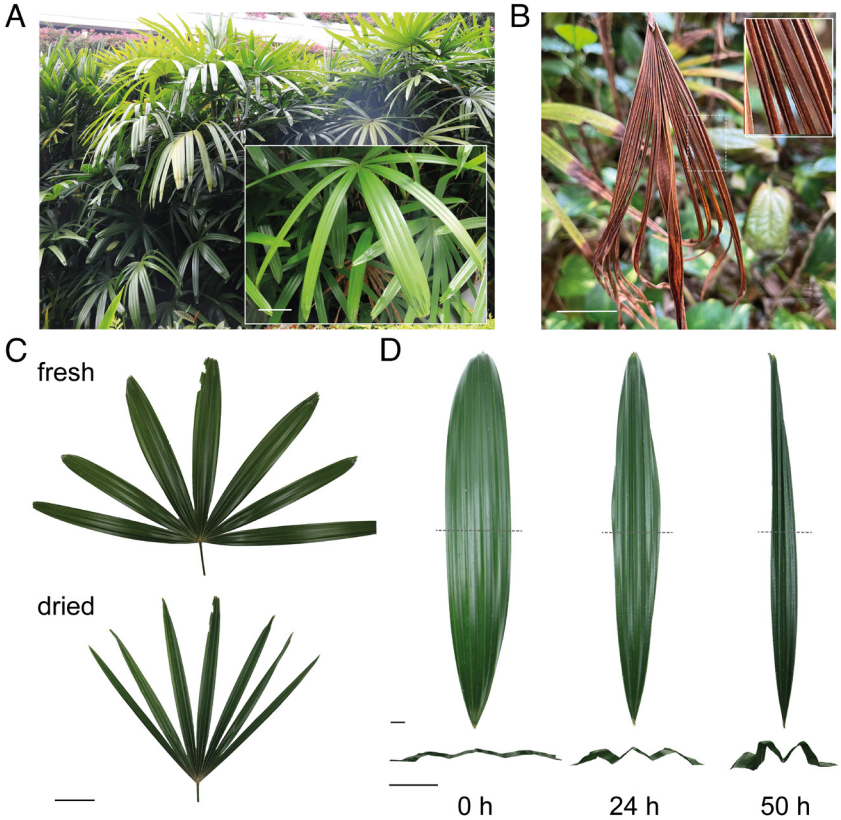

Fig. 1. Corrugated leaf folding in *R. excelsa*. (*A*) *R. excelsa*. *Inset*: A healthy frond of the plant. (*B*) A completely dried frond found in nature shows the folded morphology. The *Inset* shows the zoomed-in image of the folded leaves. (*C*) A frond of *R. excelsa* before and after air drying in the lab for 72 h. (*D*) A leaf after different periods of air drying. The *Bottom* panel shows the corresponding transverse section of the leaf. [Scale bars, 5 cm in (*A*–*C*) and 1 cm in (*D*).]

loss during drying. This allows us to establish a direct quantitative correlation between drying/evaporation and folding. How evaporation regulates the kinetics of water loss is further analyzed by considering two key mechanistic pathways—water loss from the edge and water loss from the surface—by performing controlled experiments on sections of *R. excelsa* leaves. A simple model of vapor diffusion is formulated to provide a theoretical framework to the observed kinetics of evaporative mass loss. Next, we explore the mechanical characteristics of folding through numerical simulations based on the leaf's cellular architecture. We show that volume reduction in HCs from dehydration leads to leaf folding, while alternating arrangements of HCs in the adaxial/abaxial sides result in a corrugated structure. Drawing inspiration from the folding mechanism of *R. excelsa*, we design and fabricate several autonomously hydromorphic machines made of elastomer–hydrogel hybrid materials to illustrate how biomimetic engineering benefits from the mechanistic understanding derived from plant leaf morphogenesis.

Results

Dehydration-Induced Folding. *R. excelsa* exhibits palmately compound leaves that divide into ribbed leaflets (37), as illustrated in Fig. 1*A*. Its leaves undergo corrugated folding when subjected to significant water loss. This is observed in naturally dried leaves, as shown in Fig. 1*B*, which display significant corrugation reminiscent of folded fans. Leaves artificially separated from the plant and dried under ambient laboratory conditions demonstrate a similar folded morphology (Fig. 1*C*). The fact that folding in both natural and laboratory conditions occurs slowly (taking around 72 h to transition from the freshly cut state to the dried state in Fig. 1*C*) suggests that leaf folding is passively actuated by dehydration, which occurs on a similar time scale. We note that the corrugated configuration appears to be facilitated by the direction of folding alternating between neighboring major longitudinal veins, as shown in Fig. 1*D*.

Leaves of *R. excelsa* demonstrate a flat shape with mild corrugation in the hydrated state and fold significantly under sufficient dehydration, as shown in Fig. 1. It is worth noting that the folding behavior is intrinsic and is not dependent upon the mechanical constraints from the stem, as evidenced from the experimental result that detached leaves also exhibit remarkable folding upon drying (Fig. 1*D*). To systematically quantify the evolution of the corrugated structure of the *R. excelsa*, we cut a section of length, L, from a leaf (Fig. 2*A*), and characterize the folding process in ambient air. The morphological evolution of sectional leaf samples, with different lengths, L, is recorded during the drying process. The results show the general trend that shorter leaf sections fold more quickly than longer ones. However, the final state of the leaves, e.g., after drying for 78 h, appears independent of section length.

The evolution of leaf morphology is presented in Fig. 2*A*. The folding angle, i.e., the angle formed between neighboring laminae around a hinge, θ_0, is measured as a function of the extent of dehydration or in the present context, the drying time, t. The corresponding change of folding angle ($\Delta\theta$) with time (t), representing the folding rate, is shown in Fig. 2*B*. It is seen here that the change of folding angle increases with drying time before reaching a plateau eventually (*SI Appendix*, Fig. S1). We hypothesize that longer leaf sections would take more time to attain this

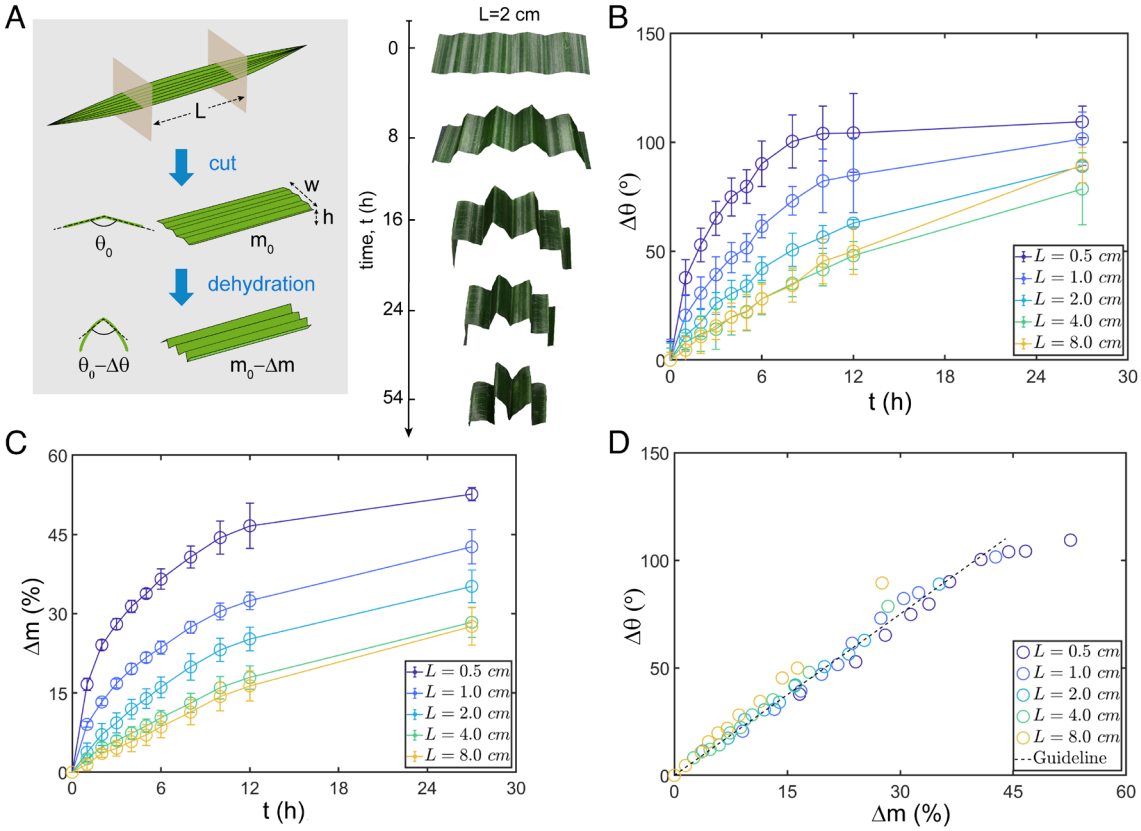

Fig. 2. Dehydration of leaf sections cut to varying lengths. (*A*) Cross-sectional shape changes of the leaf sections with drying time t for a section of length L = 2 cm. The leaves are cut according to the schematic illustration. (*B*) The change of folding angle $\Delta\theta$ with time t. $\Delta\theta$ was measured as illustrated in (*A*). (*C*) The water loss ratio, i.e., the relative reduction in sample weight, Δm with time t. See *Materials and Methods* for the calculation of Δm. (*D*) $\Delta\theta$ increases linearly with Δm. The dotted line is a guideline of the linear correlation.

plateau because of the longer duration needed for diffusion and evaporation of water during dehydration, which is supported by the experimental results in Fig. 2*B*. A theoretical framework is developed in the next section to reveal the scaling law of this timescale for shape evolution.

We further characterized the loss of water by measuring the relative reduction in sample weight, Δm, as a function of time, t (Fig. 2*C*). The results suggest that the water loss follows a similar trend to the angle change. A plot of $\Delta\theta$ against Δm (Fig. 2*D*) demonstrates a linear correlation for all leaf samples. This positive linear correlation appears universal, regardless of their length L, suggesting that dehydration directly induces the folding process. However, it is noted that in cases in which the folding duration is long and the folded leaf contacts itself (e.g., L = 0.5 cm, t = 24 h), the data points in Fig. 2*D* are not valid. From the linear relationship in Fig. 2*D*, we are able to use water loss as a proxy for the time-dependent changes in folding angle and analyze the kinetics of water loss. This approach is particularly advantageous for modeling purposes: Water loss is a more homogeneous and reproducible process in which the effect of the variations of microstructure within the leaf is averaged out (38).

Water Loss in Excised Leaves through the Edges and the Surfaces. In this section, we consider the kinetics of water loss in excised leaves to develop a general theoretical framework for a scaling law of the morphological evolution of the leaf. For excised leaf sections with width w, thickness h, length L, and open edges at $x = 0$ and $x = L$ (Fig. 2*A*), water evaporates from both the exposed edges and from the epidermis. To distinguish water loss through these two different pathways, we remove each pathway by applying water sealant (see *Insets* in Fig. 3 *A* and *B*). The amount of water loss through only the edges, which we term "edge water loss," is plotted in the *Inset* of Fig. 3*A*. By rescaling time, t, by the sample length, L, the variation of water loss ratio with time is collapsed onto a single master curve, independent of sample length.

We assume that water is uniformly distributed throughout the leaf with a relative water weight fraction, $\phi_w(t)$, at time, t, and the initial solid fraction, $\phi_s = 1 - \phi_w(0)$. For water loss from the edges, the water evaporation rate E_1 (mass per unit area per unit time) is assumed to be proportional to the water weight fraction, ϕ_w, and thus can be expressed as $E_1 = k_1 \cdot \phi_w$, where k_1 is a constant and can be determined by fitting the experimental data.

With dehydration, the mass of water in the leaf, M_w, decreases with time according to

$$\frac{dM_w}{dt} = -2whk_1\phi_w, \quad [1]$$

where wh is the cross-sectional area of the cut leaf, and factor 2 comes from there being two such cross-sections. Assuming that the density of the hydrated leaf is ρ, the initial mass of the leaf section $M_0 = \rho whL$, while $M_w = \phi_w \rho whL$. As a result, Eq. **1** can be expressed as an equation for the evolution of ϕ_w:

$$\frac{d\phi_w}{dt} = -\frac{2k_1}{\rho L}\phi_w. \quad [2]$$

Given that the initial relative water content $\phi_w(0) = 1 - \phi_s$, we find that

$$\phi_w = (1-\phi_s)\exp\left(-\frac{2k_1}{\rho L}t\right) \quad [3]$$

and the amount lost from the edge, ϕ_{loss}^{edge}, is calculated as $\phi_w(0) - \phi_w$, thus

$$\phi_{loss}^{edge} = (1-\phi_s)\left[1-\exp\left(-\frac{2k_1}{\rho L}t\right)\right]. \quad [4]$$

Eq. **4** shows that the collapse of experimental data upon scaling t/L for edge water loss corresponds to the simple assumption of uniform water distribution in the drying leaf. The change of mass due to edge water loss, Δm, as a function of t/L, is plotted in Fig. 3*A* as a dotted line, where the initial solid fraction is estimated from experiments as $\phi_s = 0.5$. It is clear that the model prediction agrees with the experimental measurements well. In *SI Appendix*, we present a more detailed model, which allows for diffusion within the leaf with a mixed boundary condition. This analysis also leads to the same scaling law and explains under what conditions the uniform water concentration approximation is valid.

For water loss through the epidermis, we assume that the evaporation rate, E_2, is related to ϕ_w by $E_2 = k_2 \cdot \phi_w$, where $k_2 \neq k_1$ is also a constant that can be fitted. Then, the mass of water in the leaf decreases with time, as

$$\frac{dM_w}{dt} = -2wLk_2\phi_w, \quad [5]$$

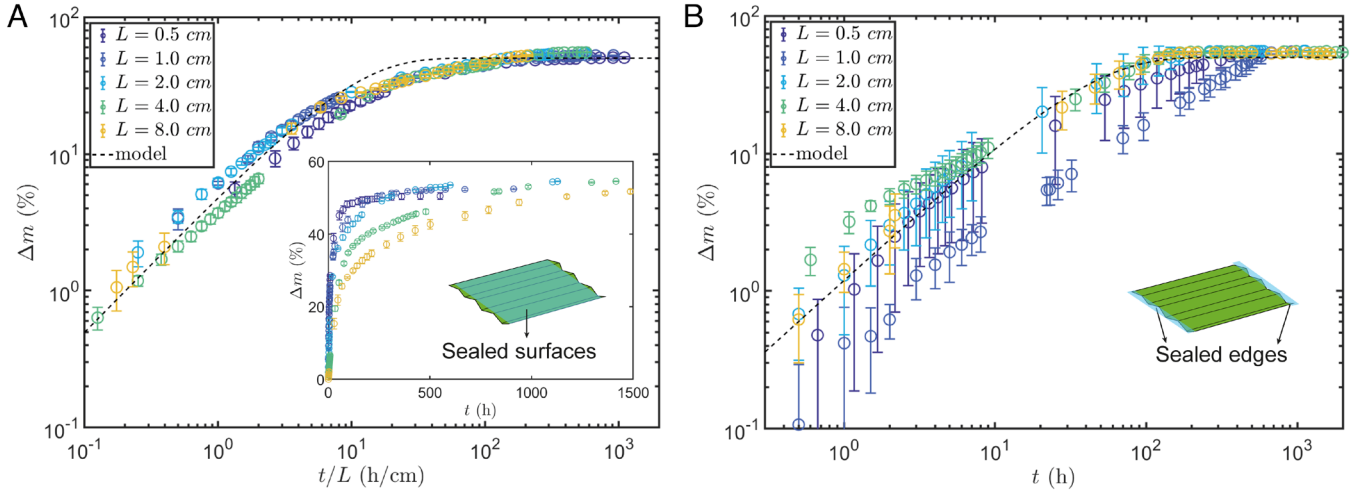

Fig. 3. Experimental measurements and theoretical model of water loss through different pathways within the leaf. (*A*) Water evaporation from the exposed edges, as illustrated by the water loss ratio (Δm) plotted as a function of the time rescaled by the sample length (t/L). The *Inset* shows the data before rescaling. (*B*) Water evaporation from the epidermis, as illustrated by Δm as a function of t. The markers indicate the mean values, the error bar represents the SD from three repeated samples, and the dashed line shows the model prediction. *Insets*: Schematic illustrations of sealing surfaces and edges.

where wL gives the surface area of the leaf. Expressing it in terms of ϕ_w, we obtain

$$\frac{d\phi_w}{dt} = -\frac{2k_2}{\rho h}\phi_w, \quad [6]$$

with the solution

$$\phi_w = (1-\phi_s)\exp\left(-\frac{2k_2}{\rho h}t\right). \quad [7]$$

The loss of water through the epidermis is

$$\phi_{loss}^{surf} = (1-\phi_s)\left[1-\exp\left(-\frac{2k_2}{\rho h}t\right)\right]. \quad [8]$$

The model suggests that water loss from the surface is independent of the cut leaf geometry (given that all leaf samples have approximately the same thickness). This is consistent with experimental measurements that the mass loss, Δm, as a function of t (again, taking $\phi_s = 0.5$) collapses onto a single master curve for different values of L (Fig. 3*B*). We note that the surface water loss for samples with small length (i.e., L = 0.5, 1 cm) shows some deviations, displaying smaller rates of water loss and larger SD. This might result from experimental errors caused by the intricacy and difficulty of applying the sealant to a small surface area.

Mechanism of Mechanical Folding. From the mechanics point of view, leaf morphogenesis is expected to be strongly dependent on nonuniform growth or heterogeneous cellular structures (4, 11). Since leaf folding upon dehydration does not involve growth, we postulate that the nonuniform cellular structure gives rise to the observed leaf folding in *R. excelsa*. By histological analysis (a more detailed description of these procedures is contained below in *Materials and Methods*), the cellular structure of the *R. excelsa* leaf can be characterized. Fig. 4*A* is an optical micrograph of the cellular structure in the transverse section of a folded leaf. A closer look at the folded region reveals the mesophylls (M), major veins (V), and folding hinges residing around the veins (Fig. 4*B*). Compared to the mesophyll cells, which appear to be distributed uniformly, cells on top of the veins are larger and more elongated in shape; we refer to these as hinge cells (HCs) (Fig. 4*B* and *SI Appendix*, Fig. S2). HCs are sometimes used to denote bulliform cells or other enlarged cells that induce rolling in grass leaves upon excessive water loss (39, 40). In the present context, we use this term to represent the role of these cells in enabling hinge-like folding. These HCs exhibit greater size changes during dehydration (compare the image of Fig. 4*B* at 0 h with that at 48 h), suggesting that they are responsible for the folding behavior. Upon drying, the differential cell shrinkage between the HCs and others may induce hinge-like folding. The position of the HCs alternates between the adaxial and abaxial sides, as indicated in Fig. 4*A*, again suggesting their importance in the corrugated folding.

Since it is difficult to measure accurately through experiments the actual change in cell size due to the large intrinsic variations in cell shape and size, we instead examine the role of HCs using finite element method (FEM) simulations. Two FEM models, as shown in Fig. 4 *C* and *D* (see more details in *Materials and Methods*), are employed to study the HC effects. Geometric parameters of the FEM models are chosen from the experimental measurements of the leaf structure. As shown in Fig. 4*C*, a structure composed of the shrinking mesophyll cells and the nonshrinking vein exhibits minimal folding even at large mesophyll strain (40%). When a hinge part is included with substantially higher shrinking than the mesophyll, the structure shows significant folding that increases with hinge strains, ϵ_{hinge} (Fig. 4*D*). We note that the normalized hinge thickness, h_{hinge}/h (see labels in Fig. 4*B*), has an influence on the effectiveness of folding with a nonmonotonic variation (see the change in folding angle, $\Delta\theta$, in Fig. 4*E*). With h_{hinge}/h around 0.6 to 0.7, folding is most significant (largest value of $\Delta\theta$) for the same hinge strain, ϵ_{hinge}. The normalized hinge thickness observed in real leaves is around 0.5 as indicated by the shaded zone in Fig. 4*E*. This suggests that real leaves exhibit an efficient hinge-folding structure close to the optimal geometry indicated by our FEM simulation results. The *Inset* in Fig. 4*E* shows the normalized $\Delta\theta$ by ϵ_{hinge} as a function of the hinge thickness, h_{hinge}/h, indicating that the nonmonotonic change of the normalized folding angle with hinge thickness is independent of the hinge strain. We also note that for $h_{hinge}/h \approx 0.5$ to 0.7, the relationship between $\Delta\theta$ and ϵ_{hinge} is approximately linear (*SI Appendix*, Fig. S3), consistent with the linear correlation between the change in folding angle and water loss observed experimentally (Fig. 2*D*).

Moreover, the dried leaf shows not only folding at the hinges but also bending of the lamina (toward the abaxial side, as displayed in Fig. 2*A*), which indicates larger shrinkage in mesophyll cells on the abaxial side than on the adaxial side. Since the distribution of mesophyll cells is relatively uniform, an explanation for this differential shrinkage could be traced to the difference in transpiration, the process of water evaporation from the surfaces of aerial organs, between the abaxial and adaxial epidermis. Stoma is the cellular apparatus for gas and water vapor diffusion through the epidermis, whose positioning on the abaxial epidermis likely leads to higher water loss in the abaxial tissues (*SI Appendix*, Fig. S6). Combining the model in Fig. 4*D* with a bilayer structure within the mesophyll region that has different shrinking ratios (see *Materials and Methods* for details), the two experimental configurations can be reproduced (Fig. 4*F*). Finally, an FEM model with multiple hinges fully reproduces the evolution of folding leaf morphologies observed in our experiments throughout the drying process (Fig. 4*G*).

Biological Function of Corrugated and Folded Morphology. The morphological and behavioral patterns seen in biological organisms are consequences of adaptation to their environment over the long history of evolution. The palms, an ancient family of angiosperms mostly found in tropical rainforests, mainly reside in the shaded mid- or understory of the rainforests (41). The environment leads to the development of some distinctive traits in palm leaves—broad or even gigantic, tough, and often ribbed or mildly corrugated (42). The behavior of corrugated folding in response to dehydration of *R. excelsa* may also have potential advantages for their survival.

First, while most leaves droop down and exhibit a loss of their mechanical rigidity when subjected to dehydration due to a reduction in turgor pressure, corrugated folding upon dehydration could be a mechanism that mitigates the disadvantages of losing rigidity by retaining the structural integrity of the leaves. For example, maintaining the rigidity may facilitate the collection and preservation of water droplets on the leaf adaxial surface from rain or water vapor condensation since the adaxial surface of *R. excelsa* is hydrophilic, as indicated by the small contact angle (*SI Appendix*, Fig. S4*A*). Water droplets can be absorbed onto the leaf surface without sliding (*SI Appendix*, Fig. S4*B*), and they leave residues when forced to slide off from the surface (*SI Appendix*, Fig. S4*C*), implying the capability of the leaf to collect water on its surface. To demonstrate the modulation of rigidity, we conduct three-point bending tests to measure the bending stiffness of the *R. excelsa* leaf both before and after folding (Fig. 5*A*). Compared to the fresh ones (t = 0), leaf sections dried for t = 4 h demonstrate higher resistance to bending, which is indicated by the larger initial slopes (i.e., the bending stiffness), k, on the force–displacement curves.

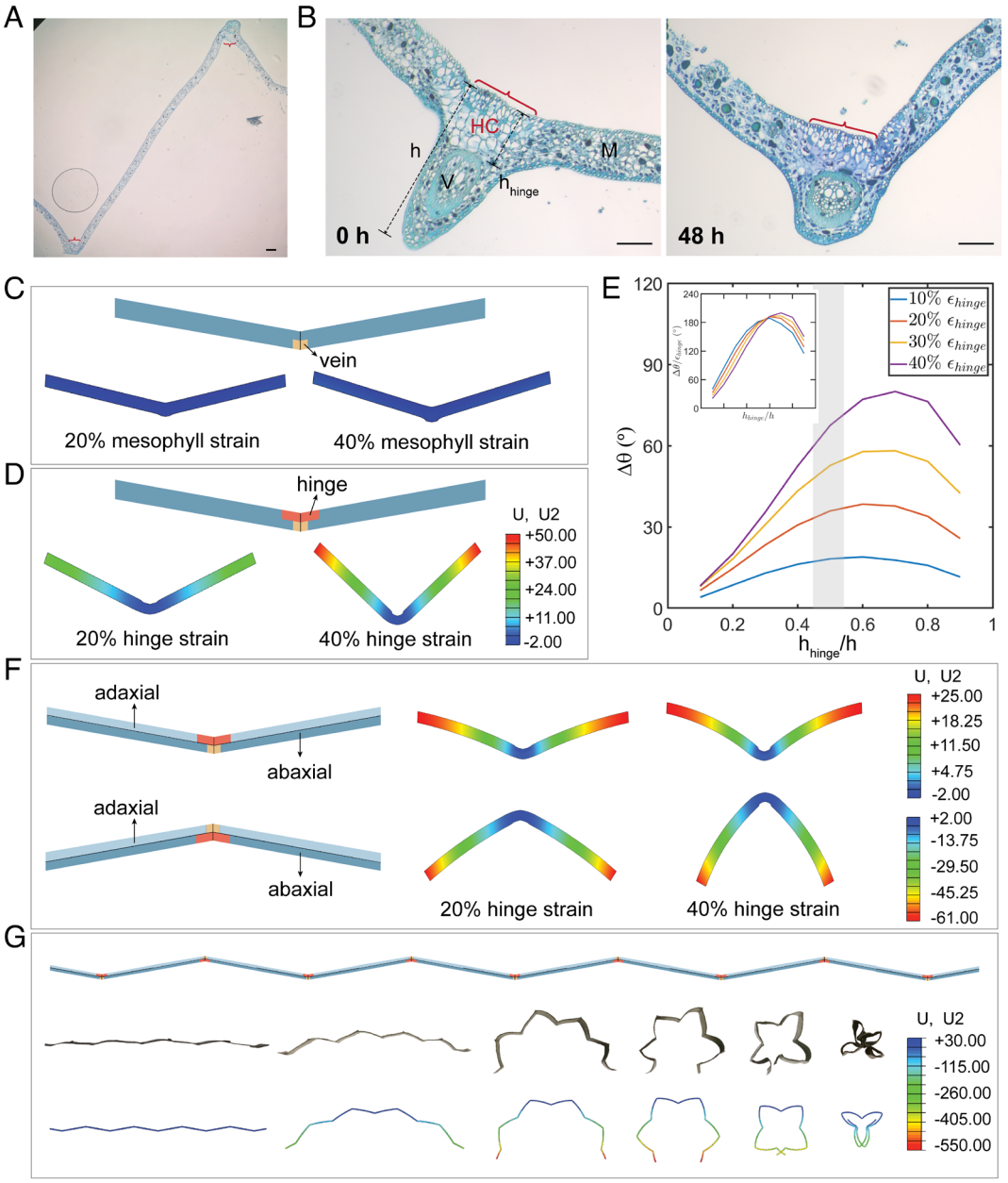

Fig. 4. Folding mechanism of *R. excelsa*. (*A*) Optical micrograph of the transverse section of the leaf. (Scale bar, 100 μm.) Red curly braces denote the location of the HCs, the same as in (*B*). (*B*) Zoomed-in micrographs of the folding hinge before (*Left*) and after (*Right*) dehydration for 48 h. (Scale bar, 100 μm.) M, mesophyll cells. V, vein. HC, hinge cells. The hinge thickness, h_{hinge}, and total thickness of the hinge, h, are indicated on the micrograph. (*C*) FEM simulations of folding without the hinge structure. *Top*, 2D model configuration composed of the mesophyll region (blue) and the vein region (yellow). *Bottom*, contour plots of deformed structures at 20% and 40% mesophyll strains. (*D*) FEM simulations of folding with hinges. *Top*, 2D model configuration composed of the mesophyll region (blue), the vein region (yellow), and the hinge region (red). *Bottom*, contour plots of deformed structures at 20% and 40% hinge strains. The color map indicates the displacement in the x_2 (vertical) direction for the contour plots in (*C*) and (*D*). (*E*) The effect of hinge thickness on folding, plotted as the change of folding angle $\Delta\theta$ as a function of the normalized hinge thickness h_{hinge}/h at various hinge strains ϵ_{hinge}. The shaded region indicates the approximate range of hinge thickness from experimental observations. The *Inset* shows the change of folding angle scaled by the hinge strain. (*F*) FEM simulations of hinge folding combined with bending of mesophyll part by incorporating the adaxial and abaxial bilayer that have differential shrinking properties. The model configurations are shown on the *Left* and the deformed shapes at 20% and 40% hinge strains are shown on the *Right*. (*G*) The folding process with multiple hinges. *Top*, the FEM model configuration. *Bottom*, cross sections of sectioned leaves (L = 2 cm) at increasing dehydration times with the corresponding FEM simulation with increasing hinge strain that reproduces the folded leaf morphologies.

The leaf sections dried for t = 8 h display even higher rigidity. These measurements demonstrate that folding of leaves into corrugated shapes upon drying (Figs. 2 *A* and *B* and 4) significantly enhances their structural rigidity. This is consistent with the analysis for simple curved strips (43).

Second, to investigate the potential roles of shape-morphing in leaf water loss, we experimentally measured and compared the rate of water loss in leaves under different conditions, as shown in Fig. 5*B* and *SI Appendix*, Fig. S5. The control group is dried without any mechanical constraint, allowing natural folding and curling, while the constrained group is manually restrained from folding and curling using wooden sticks to keep the leaf blade flat throughout the dehydration process. Interestingly, the control group exhibits a significantly lower rate of water loss than the constrained group. The result suggests that the natural shape changes of the leaf, i.e., folding together with curling, may effectively mitigate water loss, protecting the leaves from unfavorable environments for survival. We postulate that the rate of water loss through the epidermis might be modulated by the mechanical stress in the tissues, especially the tensile stress in the epidermis caused by the

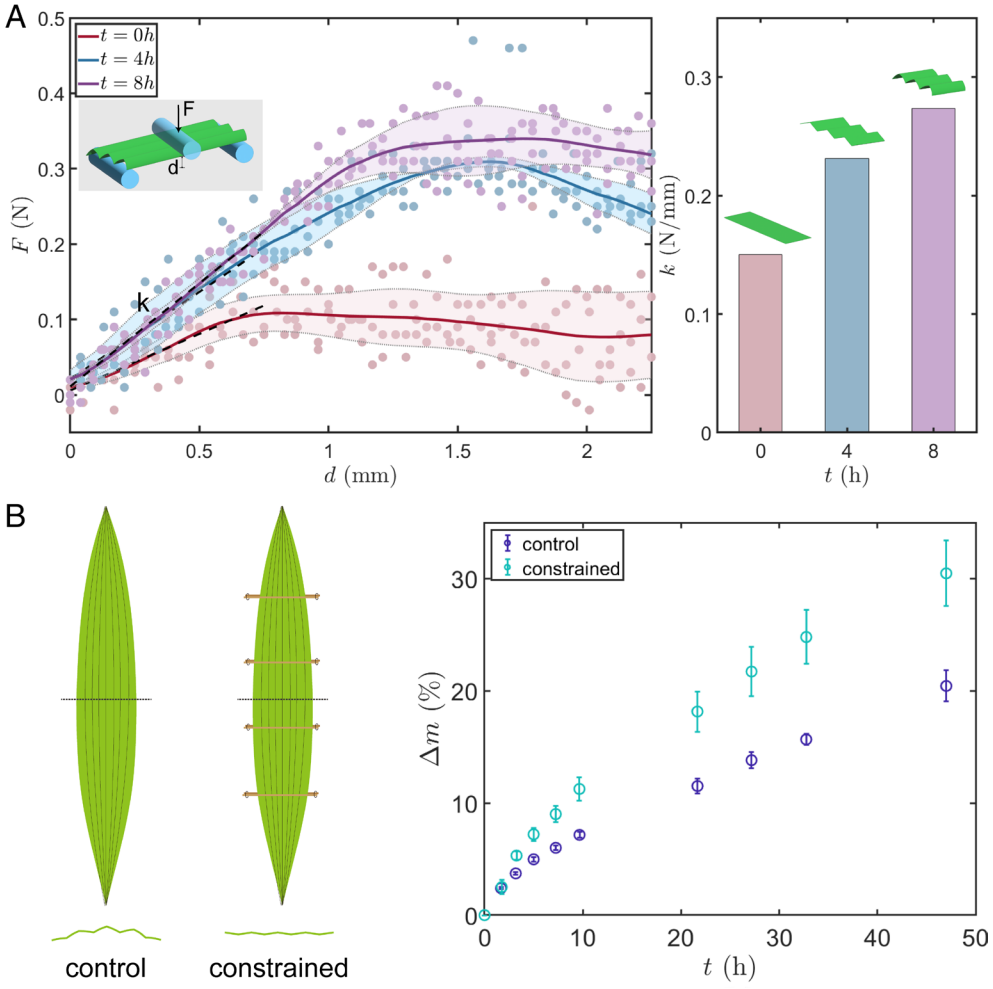

Fig. 5. Folding-related biological functions. (*A*) Leaf folding increases its bending rigidity. The *Left* panel shows the force–deflection curves in three-point bending tests of the leaf after 0, 4, and 8 h of drying. The *Inset* shows the schematic setup of the three-point bending test. The *Right* panel shows the bending rigidity (*k*) under different drying times. (*B*) Constrained leaf drying experiment. *Left*, schematics showing the control and constrained conditions with the corresponding cross-sectional shapes. *Right*, measurements of water loss ratio for the control and constrained samples. The circles indicate the mean values of three replicates, while the error bars indicate SD.

external constraints, exerting on the various cellular structures on the leaf epidermis (*SI Appendix*, Fig. S6). However, the mechanisms underlying the observed differences in water loss are likely to be more complicated and remain to be fully investigated.

Biomimetic Foldable Soft Machines. The realization of controllable folding mechanisms that produce complex shape changes by recourse to autonomous hygromorphing responses has been widely explored. For example, folding is demonstrated in sheets of paper made of plant-based pollen on which a second layer of patterned lines was deposited to induce differential expansion within the bilayer (14, 20, 21). Here, we demonstrate how a simple folding mechanism, such as that found in the leaf of *R. excelsa*, can serve as a model for the development of biomimetic hydroresponsive foldable machines for potential applications in flexible electronics and soft robotics. To illustrate these biomimetic concepts, we design hinge-based hybrid structures where the hinges are made of hydrogel and the base is made of an elastomer. The hydrogel exhibits significant volume change when the relative humidity (RH) varies, while the elastomer has a relatively stable volume. Bonding the two materials together leads to strain mismatch upon dehydration. As a proof of concept, we fabricate hinge-based foldable thin plates that show autonomous morphing in response to dehydration/rehydration (Fig. 6).

Here, based on the mechanism of differential shrinking, we create a hinge-folding device (Fig. 6 *A*, i and ii) in which the folding angle is dependent on the RH of the environment, thus potentially serving as a humidity sensor. The angle change of the device is large within the high, 80 to 100% RH range (Fig. 6 *A*, iii). As illustrated in *SI Appendix*, Fig. S7, the increase of folding angle of the device could be approximately predicted by the mathematical model proposed in the previous section, i.e., $\Delta\theta = b \cdot \left[1 - exp(-t/k)\right]$, where b and k are fitting parameters, analogous to the model of water loss in the leaf sections (Fig. 3). Utilizing the same principle, foldable structures with more complex geometries can be achieved. Fig. 6*B* demonstrates a hydroresponsive foldable umbrella that folds when dried and opens up when soaked in water. Note that the folding speed during dehydration (Fig. 6 *B*, i to iii) is about 40 times slower than the opening speed when soaked in water (Fig. 6 *B*, iv to vi), enabling swift deployment when needed and gradual restoration back to the folded state. This is an example of a responsive actuator that can potentially be used in soft robotics applications (13, 44).

Discussion

The majority of shape-morphing components in plants, among them many leaves, undergo gentle curving in response to external

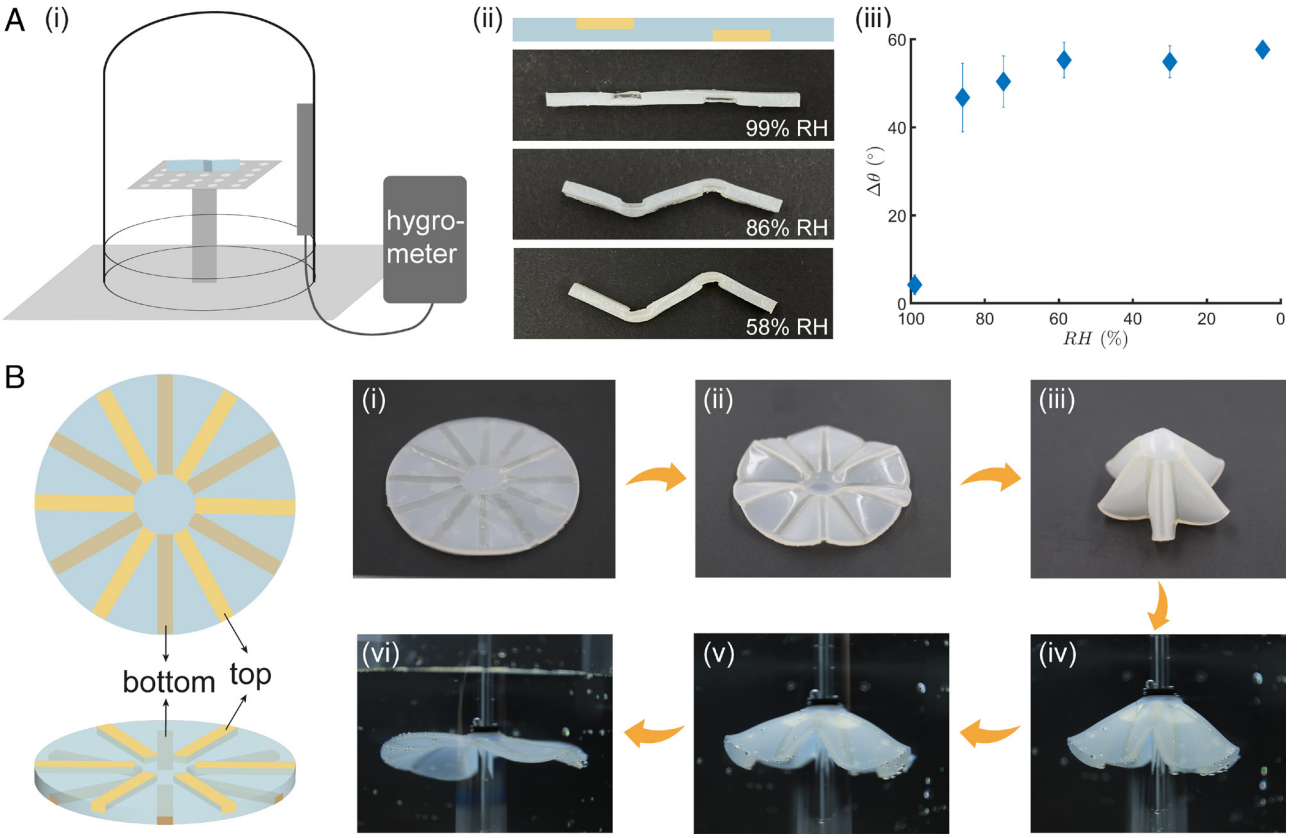

Fig. 6. Biomimetic folding machines made by the Ecoflex–hydrogel composite. (*A*) Humidity sensor. (i) Experimental setup for the drying chamber of the humidity sensors. (ii) Schematic of the folding device and the folded device after drying under different RH for 24 h. (iii) Decrease in the folding angle, $\Delta\theta$, from the initial configuration (θ_0 = 180°) after drying under various RHs for 24 h. (*B*) *Left*, schematic design of the soft umbrella machine. (i–vi) Morphing of the soft umbrella machine. (i–iii) Folding of the umbrella upon drying in laboratory ambient conditions. (iv–vi) Unfolding of the umbrella upon immersion in water.

stimulation. Sharp folding is an exception rather than the norm. On the other hand, in engineered structures, sharp folding is often achieved by incorporating complex hinge mechanisms (45), or by producing origami lines (46), or through local buckling/crumbling (4, 47). In this work, we employ a multifaceted approach combining experimental characterization, mechanical analysis, and mathematical modeling to study the morphing mechanism of the leaf of the palm species *R. excelsa*, specifically its corrugated folding upon dehydration. Our quantitative analysis of the kinetics of water loss accurately predicts the trend of water evaporation from either the epidermis or the exposed cuts of sectioned leaves. The simplicity of the model assumptions and the resulting scaling laws can potentially be applied to general water loss in leaves of other species. Furthermore, our experiments reveal the importance of the shrinking of HCs in dehydration-induced sharp folding. We demonstrate that simple mechanical and mathematical rules can accurately capture the mechanistic trends observed in many the seemingly sophisticated behaviors of biological systems.

A fundamental question that remains to be explored is the structural characteristic that allows HCs to exhibit larger volume change compared to other cells. First, there might be cytoskeletal patterns that facilitate cell deformation, as the cytoskeletal arrangement could indicate microfibril orientation and lead to cell wall anisotropy (48). Prior studies on other plants have identified the roles of coordinated cell wall anisotropy in the actuation mechanism of motor cells. For example, the pulvini of Mimosa are anisotropically reinforced by aligned cellulose microfibrils that result in nonuniform tissue shrinking in response to turgor change (27). Similar mechanisms are found in the morphing of *Dandelion pappus* (49), *Cardamine hirsuta* (50), etc. The HCs of *R. excelsa* might also exhibit a certain degree of cell wall anisotropy, enhancing their capability of deformation in the transverse direction and creating strain mismatch. Second, these HCs, displaying larger size than the neighboring cells (*SI Appendix*, Fig. S2), are similar to the hydration-regulated bulliform cells that display significantly excess shrinking in dehydration in leaves of the grass families (40). The excess shrinking of bulliform cells is often accounted for by their large sizes and thin walls. The large sizes and thin walls may together modulate the effective modulus of the cell, changing the cell deformability. Described by the elastic part of Ortega equation (51, 52), the rate of volume change of a plant cell bearing a uniform turgor pressure is $(1/V)\cdot(dV/dt) = (1/E)\cdot(dP/dt)$, where V is the volume of the cell, E is the effective (volumetric) elastic modulus of the cell, and P is the turgor pressure. Cells with larger sizes (thus smaller wall-to-volume ratio) or with thinner walls have lower effective moduli since they are less resistive to deformation (53, 54). Moreover, we expect the turgor change to remain constant between neighboring cells because any turgor difference would induce flow of water to balance it. Therefore, given the same dP/dt, we expect larger cells to demonstrate greater volume change because of their lower moduli. Future studies could explore the cell wall thickness and cytoskeletal structures of the HCs to investigate the mechanism of larger volume change of HCs.

The observation of corrugated folding in the leaf of *R. excelsa* not only serves as an intriguing natural phenomenon but also offers insights into potential strategies for achieving sharp folding in engineered systems. The leaf structure suggests that this may be achieved by integrating heterogeneous materials design at the

intrastructural level, with different material properties or cellular structures that exhibit distinct strains in response to environmental cues (15, 55). One such design can be found in the device developed in this study, which demonstrates the feasibility of achieving folding through the process of water evaporation. By strategically integrating these materials into the machine's architecture, precise and reversible folding in soft materials could potentially be achieved through controlled moisture exposure and geometrical design (56). Such strategies based on the understanding of sharp folding in plants have the potential to influence the engineering design of morphing structures.

Materials and Methods

Sample Collection and Preparation. The leaves of *R. excelsa* were collected on NTU campus. The leaves were cut from the frond along the line where leaves are naturally split (Fig. 1) and allowed to dry in air at ambient laboratory conditions (25 °C, 60% RH).

Measurement of the Leaf Dehydration Process. The cross-sectional profiles of the whole and sectioned leaves were obtained by scanning the leaf using a digital microscope (Keyence VHX-7000) after different periods of drying (Figs. 1*D* and 2*A*). The folding angle of a sample was measured using ImageJ as the mean folding angle of all hinges in the sample. For sectioned leaves, leaves were cut from their middle part into sections of various lengths, L, and allowed to dry (Fig. 2). Meanwhile, samples were weighed using an analytical balance at each drying time. Three replicate samples were measured and averaged. At the initial state, the sample was naturally hydrated, and the initial mass ratio and initial folding angle is denoted as m_0 (i.e., $m_0 = 1$) and θ_0, respectively (Fig. 2*A*). At time t, the mass ratio of the sample decreases by Δm, denoting the water loss ratio, calculated as $(M_0 - M_t)/M_0$, where M_0 and M_t are the mass at the initial state and at drying time t, respectively. The folding angle decreases by $\Delta\theta$.

To compare the water loss through the cut ends and that through the epidermis, we performed sealing on the leaf sections (Fig. 3, *Inset* illustrations) using petroleum jelly (Vaseline) as the water sealant. The sealant was carefully applied to either the cut ends or the epidermis of the samples using a cotton bud. The mass of the sealant applied was subtracted from the weight measurements to obtain the sample weights upon drying. Three replicate samples were measured and averaged. The water loss ratio Δm is calculated the same way as described above. The dotted curves in Fig. 3 *A* and *B* were fitted curves of all experimental data using Eqs. **4** and **8**, respectively. The fitting constants obtained were $c_1 = 2k_1/(\rho h) = 0.1$ and $c_2 = 2k_2/(\rho h) = 0.024$.

Characterization of Microstructures. To examine the cross-sectional cellular structure (Fig. 4 *A* and *B*), leaf tissues of 5 mm × 2 mm size were cut from the midsection of the leaf at the desired drying time, fixed in methanol/ethanol, and cut to thin sections of 7 μm using a cryostat (Leica RM2155). The sections were then stained using 0.5% toluidine blue O (Sigma-Aldrich) and cleared using HistoChoice Clearing Agent (Sigma-Aldrich), and coverslipped for further examination under the optical microscope (Olympus BA15XL; Tucsen FL-20). The epidermis microstructures (*SI Appendix*, Fig. S6) were observed using a digital microscope (Keyence VHX-7000).

FEM Simulation of the Leaf-Folding Process. Numerical simulations were conducted using the commercial finite element analysis software ABAQUS to simulate the folding behavior. The model was constructed as a 2D shell model, where the element type used was CPE4R. The boundary conditions are that the midline of the model was set to zero displacement in the x_1 (horizontal) direction and that the end point of the midline was set to be fixed. Linear elastic constitutive relation was applied with the following ABAQUS material constants: Young's modulus $E_{base} = E_{hinge} = 60$ MPa, $E_{vein} = 1{,}000$ MPa; Poisson's ratio $\nu_{base} = \nu_{hinge} = 0.4$, $\nu_{vein} = 0.45$; expansion coefficient $\alpha_{base} = 1E\text{-}05$, $\alpha_{hinge} = 1E\text{-}03$, $\alpha_{vein} = 1E\text{-}10$. Various temperature fields, T, were uniformly imposed on the model. Differences in the expansion coefficients, α, between different materials result in differential thermal strains, $\varepsilon = \alpha T$. The base sections in the above model were further divided into two layers (Fig. 4*F*) with the same mechanical properties but different expansion coefficients, $\alpha_{ad} = 1E\text{-}05$, $\alpha_{ab} = 1E\text{-}04$, corresponding to the adaxial and abaxial tissues in the leaves. The multihinge model (Fig. 4*G*) was constructed by replicating the single-hinge model (Fig. 4*F*) and connecting them along the edges using tied constraints.

Three-Point Bending Tests of the Leaves. The load–displacement curves of the leaves were measured using a mechanical tester (Mark-10 F305) with a force sensor of 25 N. The samples, 2 cm in width and 8 cm in length, were simply supported at both ends by cylindrical rods with a radius of 5 mm. The load was applied to the center of the samples (Fig. 5 *A*, *Inset*). The separation distance between two supports is kept at 8 cm for all measurements. The displacement loading speed is 5 mm/min, and data were recorded at a frequency of 2 Hz.

Constrained Leaf Morphing and Dehydration Process. Leaves were cut from the plant and the petiole was kept in water before the start of the measurement. The rates of water loss in leaves were compared under the control and the constrained conditions (Fig. 5*B*). i) Leaves in the control group were allowed to dehydrate in their natural shape without external constraint. ii) Leaves in the constrained group were each constrained between two wooden sticks which are fixed at both ends. The constrained leaves do not exhibit folding or curling throughout the dehydration measurement. Three replicate samples were measured and averaged for each group. All leaf samples were hanging from their distal ends with tips clipped in the ambient condition (25 °C, 60% RH) (*SI Appendix*, Fig. S5).

Fabrication of the Biomimetic Self-Folding Machines. The hydrogel precursor was made by mixing acrylamide (12 wt.%), bis-acrylamide (19:1), Irgacure 2959 (0.1 wt.% of acrylamide), and sodium alginate (8 wt.%). The Ecoflex (Smooth-On 00-10) base was mold-casted into the designed structure that constitutes the nondeformable parts and cured for 20 min in 60 °C oven. To allow bonding between Ecoflex and hydrogels, Ecoflex was surface treated using benzophenone (57) before depositing hydrogel. Then, the hydrogel precursor was cast into the hinge regions of the Ecoflex mold and cured in UV flood. The cured hybrid structure was then allowed to dehydrate in a humidity-controlled chamber (Fig. 6*A*) or in lab ambient conditions (25 °C, 60% RH) (Fig. 6*B*). RH of the chamber is controlled by using saturated salt solutions, which are potassium sulfate, potassium chloride, sodium chloride, sodium bromide, magnesium chloride, and lithium bromide for 99%, 86%, 75%, 58%, 30%, and 6% RHs, respectively. Three replicates were measured for each condition. The folding angle for each hinge was measured using ImageJ and averaged over all samples to obtain the mean folding angle. The humidity sensor in Fig. 6*A* has a dimension of 3 mm × 3 mm × 60 mm, with two hinges of 1.5 mm × 3 mm × 8 mm. The self-folding umbrella in Fig. 6*B* has a radius of 45 mm and thickness of 2 mm. Six hinges with dimension 1 mm × 5 mm × 35 mm were uniformly arranged along the radial directions. The change of folding angle in *SI Appendix*, Fig. S7, was recorded every 15 min over a total time of 24 h, and the data shown are averaged among three replicates.

Data, Materials, and Software Availability. All study data are included in the article and/or *SI Appendix*.

ACKNOWLEDGMENTS. K.G. acknowledges the support of the Nanyang President's Graduate Scholarship from Nanyang Technological University, Singapore. M.L. acknowledges the Presidential Postdoctoral Fellowship from Nanyang Technological University, Singapore, and start-up funding from the University of Birmingham, UK. K.J.H. acknowledges financial support from Nanyang Technological University, Singapore (Grant M4082428), and the Ministry of Education, Singapore, under its Academic Research Fund Tier 3 (Grant MOE-MOET32022-0002).

Author affiliations: [a]School of Mechanical and Aerospace Engineering, Nanyang Technological University, Singapore 639798, Singapore; [b]Department of Mechanical Engineering, University of Birmingham, Birmingham B15 2TT, United Kingdom; [c]Mathematical Institute, University of Oxford, Oxford OX2 6GG, United Kingdom; [d]Division of Engineering, Brown University, Providence, RI 02912; [e]Department of Materials Science and Engineering, Massachusetts Institute of Technology, Cambridge, MA 02139; and [f]School of Chemistry, Chemical Engineering and Biotechnology, Nanyang Technological University, Singapore 639798, Singapore

1. K. Jonsson, Y. Ma, A.-L. Routier-Kierzkowska, R. P. Bhalerao, Multiple mechanisms behind plant bending. *Nat. Plants* **9**, 13–21 (2023).
2. D. Briggs, S. M. Walters, *Plant Variation and Evolution* (Cambridge University Press, 2016).
3. T. Givnish, "On the adaptive significance of leaf form" in *Topics in Plant Population Biology* (Springer, 1979), pp. 375–407.
4. K. Guo, C. Huang, Y. Miao, D. J. Cosgrove, K. J. Hsia, Leaf morphogenesis: The multifaceted roles of mechanics. *Mol. Plant* **15**, 1098–1119 (2022).
5. K. Song, E. Yeom, S. J. Lee, Real-time imaging of pulvinus bending in *Mimosa pudica*. *Sci. Rep.* **4**, 6466 (2014).
6. Y. Forterre, J. M. Skotheim, J. Dumais, L. Mahadevan, How the Venus flytrap snaps. *Nature* **433**, 421–425 (2005).
7. A. Rafsanjani, V. Brulé, T. L. Western, D. Pasini, Hydro-responsive curling of the resurrection plant *Selaginella lepidophylla*. *Sci. Rep.* **5**, 8064 (2015).
8. H. Wang, E. T. Nilsen, M. Upmanyu, Mechanical basis for thermonastic movements of cold-hardy Rhododendron leaves. *J. R. Soc. Interface.* **17**, 20190751 (2020).
9. H. Quan, D. Kisailus, M. A. Meyers, Hydration-induced reversible deformation of biological materials. *Nat. Rev. Mater* **6**, 264–283 (2021).
10. R. J. Morris, M. Blyth, How water flow, geometry, and material properties drive plant movements. *J. Exp. Bot.* **70**, 3549–3560 (2019).
11. C. Huang, Z. Wang, D. Quinn, S. Suresh, K. J. Hsia, Differential growth and shape formation in plant organs. *Proc. Natl. Acad. Sci. U.S.A.* **115**, 12359–12364 (2018).
12. R. Ohlendorf, N.Y.-H. Tan, N. Nakayama, Engineering themes in plant forms and functions. *Annu. Rev. Plant Biol.* **74**, 777–801 (2023).
13. S. Coyle, C. Majidi, P. LeDuc, K. J. Hsia, Bio-inspired soft robotics: Material selection, actuation, and design. *Extreme Mech. Lett.* **22**, 51–59 (2018).
14. M. J. Motala *et al.*, Programming matter through strain. *Extreme Mech. Lett.* **3**, 8–16 (2015).
15. G. Cai, J.-H. Ciou, Y. Liu, Y. Jiang, P. S. Lee, Leaf-inspired multiresponsive MXene-based actuator for programmable smart devices. *Sci. Adv.* **5**, eaaw7956 (2019).
16. M. Liu, L. Domino, D. Vella, Tapered elasticæ as a route for axisymmetric morphing structures. *Soft Matter* **16**, 7739–7750 (2020).
17. M. Liu, L. Domino, I. Dupont de Dinechin, M. Taffetani, D. Vella, Snap-induced morphing: From a single bistable shell to the origin of shape bifurcation in interacting shells. *J. Mech. Phys. Solids* **170**, 105116 (2023).
18. Y. Wang *et al.*, Insect-scale jumping robots enabled by a dynamic buckling cascade. *Proc. Natl. Acad. Sci. U.S.A.* **120**, e2210651120 (2023).
19. T.-F. Fan *et al.*, Transformation of hard pollen into soft matter. *Nat. Commun.* **11**, 1449 (2020).
20. Z. Zhao *et al.*, Actuation and locomotion driven by moisture in paper made with natural pollen. *Proc. Natl. Acad. Sci. U.S.A.* **117**, 8711–8718 (2020).
21. Z. Zhao *et al.*, Digital printing of shape-morphing natural materials. *Proc. Natl. Acad. Sci. U.S.A.* **118**, e2113715118 (2021).
22. Z. Zhao *et al.*, Recyclable and reusable natural plant-based paper for repeated digital printing and unprinting. *Adv. Mater.* **34**, 2109367 (2022).
23. Y. Hwang *et al.*, Plant-based substrate materials for flexible green electronics. *Adv. Mater. Technol.* **7**, 2200446 (2022).
24. J. R. Philip, Plant water relations: Some physical aspects. *Annu. Rev. Plant Physiol.* **17**, 245–268 (1966).
25. J. Dumais, Y. Forterre, "Vegetable Dynamicks": The role of water in plant movements. *Annu. Rev. Fluid Mech.* **44**, 453–478 (2012).
26. N. Moran, Osmoregulation of leaf motor cells. *FEBS Lett.* **581**, 2337–2347 (2007).
27. D. A. Sleboda, A. Geitmann, R. Sharif-Naeini, Multiscale structural anisotropy steers plant organ actuation. *Curr. Biol.* **33**, 639–646.e3 (2023).
28. F. Zhang *et al.*, Unperceivable motion mimicking hygroscopic geometric reshaping of pine cones. *Nat. Mater.* **21**, 1357–1365 (2022).
29. J. Ha *et al.*, Hygroresponsive coiling of seed awns and soft actuators. *Extreme Mech. Lett.* **38**, 100746 (2020).
30. R. Elbaum, L. Zaltzman, I. Burgert, P. Fratzl, The role of wheat awns in the seed dispersal unit. *Science* **316**, 884–886 (2007).
31. L. Ren *et al.*, Plant-morphing strategies and plant-inspired soft actuators fabricated by biomimetic four-dimensional printing: A review. *Front. Mater.* **8**, 651521 (2021).
32. X. Yang *et al.*, Morphing matter: From mechanical principles to robotic applications. *Soft Sci.* **3**, 38 (2023).
33. I. Andrade-Silva, M. Adda-Bedia, M. A. Dias, Foldable cones as a framework for nonrigid origami. *Phys. Rev. E* **100**, 033003 (2019).
34. T. Jules, F. Lechenault, M. Adda-Bedia, Local mechanical description of an elastic fold. *Soft Matter* **15**, 1619–1626 (2019).
35. L. Li *et al.*, Overexpression of ACL1 (abaxially curled leaf 1) increased bulliform cells and induced abaxial curling of leaf blades in rice. *Mol. Plant* **3**, 807–817 (2010).
36. J. M. Alvarez, J. F. Rocha, S. R. Machado, Bulliform cells in *Loudetiopsis chrysothrix* (Nees) Conert and *Tristachya leiostachya* Nees (Poaceae): Structure in relation to function. *Braz. Arch. Biol. Technol.* **51**, 113–119 (2008).
37. D. R. Kaplan, N. G. Dengler, R. E. Dengler, The mechanism of plication inception in palm leaves: Problem and developmental morphology. *Can. J. Bot.* **60**, 2939–2975 (1982).
38. M. Liu, J. Wu, Y. Gan, D. A. H. Hanaor, C. Q. Chen, Tuning capillary penetration in porous media: Combining geometrical and evaporation effects. *Int. J. Heat Mass Transfer* **123**, 239–250 (2018).
39. M. B. Kirkham, *Principles of Soil and Plant Water Relations* (Elsevier, 2023).
40. S. Matschi *et al.*, Structure-function analysis of the maize bulliform cell cuticle and its potential role in dehydration and leaf rolling. *Plant Direct* **4**, e00282 (2020).
41. T. L. Couvreur, W. J. Baker, Tropical rain forest evolution: Palms as a model group. *BMC Biol.* **11**, 48 (2013).
42. H. E. Moore, N. W. Uhl, Major trends of evolution in palms. *Bot. Rev.* **48**, 1–69 (1982).
43. M. Taffetani, F. Box, A. Neveu, D. Vella, Limitations of curvature-induced rigidity: How a curved strip buckles under gravity. *EPL* **127**, 14001 (2019).
44. Y. Lee, W. J. Song, J.-Y. Sun, Hydrogel soft robotics. *Mater. Today Phys.* **15**, 100258 (2020).
45. X. Liu *et al.*, Recent advances in stimuli-responsive shape-morphing hydrogels. *Adv. Funct. Mater.* **32**, 2203323 (2022).
46. D. Rus, M. T. Tolley, Design, fabrication and control of origami robots. *Nat. Rev. Mater.* **3**, 101–112 (2018).
47. F. Xu, C. Fu, Y. Yang, Water affects morphogenesis of growing aquatic plant leaves. *Phys. Rev. Lett.* **124**, 038003 (2020).
48. D. J. Cosgrove, Building an extensible cell wall. *Plant Physiol.* **189**, 1246–1277 (2022).
49. M. Seale *et al.*, Dandelion pappus morphing is actuated by radially patterned material swelling. *Nat. Commun.* **13**, 2498 (2022).
50. H. Hofhuis *et al.*, Morphomechanical innovation drives explosive seed dispersal. *Cell* **166**, 222–233 (2016).
51. J. K. E. Ortega, Augmented growth equation for cell wall expansion 1. *Plant Physiol.* **79**, 318–320 (1985).
52. J. K. E. Ortega, Dimensionless numbers to analyze expansive growth processes. *Plants* **8**, 17 (2019).
53. D. Vella, A. Ajdari, A. Vaziri, A. Boudaoud, Indentation of ellipsoidal and cylindrical elastic shells. *Phys. Rev. Lett.* **109**, 144302 (2012).
54. A. Lazarus, H. C. B. Florijn, P. M. Reis, Geometry-induced rigidity in nonspherical pressurized elastic shells. *Phys. Rev. Lett.* **109**, 144301 (2012).
55. J. Zhao, J. Bae, Microphase separation-driven sequential self-folding of nanocomposite hydrogel/elastomer actuators. *Adv. Funct. Mater.* **32**, 2200157 (2022).
56. C. Ni *et al.*, Shape memory polymer with programmable recovery onset. *Nature* **622**, 748–753 (2023).
57. H. Yuk, T. Zhang, G. A. Parada, X. Liu, X. Zhao, Skin-inspired hydrogel–elastomer hybrids with robust interfaces and functional microstructures. *Nat. Commun.* **7**, 12028 (2016).